Computers and Electrical Engineering 120 (2024) 109730

Contents lists available at ScienceDirect

Computers and Electrical Engineering

journal homepage: www.elsevier.com/locate/compeleceng

Data-driven assessment of VI diagrams for inference on pantograph quantities waveform distortion in AC railways ☆

Rafael S. Salles [a,*], Roger A. De Oliveira [a], Sarah K. Rönnberg [a], Andrea Mariscotti [b]

[a] Electric Power Engineering Group, Luleå University of Technology, Skellefteå, 93187, Sweden
[b] Department of Electrical, Electronics and Telecommunication Engineering and Naval Architecture (DITEN), University of Genoa, Genoa, 16145, Italy

ARTICLE INFO

Keywords:
Dimension reduction
Pattern analysis
Power quality
Power system harmonics
Load monitoring
Guideway transportation

ABSTRACT

This work proposes an application of unsupervised deep learning (DL) on 2-D images containing VI diagrams of measured railway pantograph quantities to find patterns in operating conditions (OCs) and waveform distortion. Measurement data consist of pantograph voltage and current measurements from a Swiss 15 kV 16.7 Hz commercial locomotive and a French 2x25 kV 50 Hz test-dedicated locomotive, containing more than 4000 records of 5-cycle snippets for each system. The variational autoencoder (VAE), followed by feature clustering, finds patterns in the input data. Each cluster captures patterns from the VI diagrams, which contain information from current and voltage waveshapes and sub-second variations. The time-domain admittance allows inference about the rolling stock (RS) operation and the waveform distortion spectra, including harmonics and supraharmonics characteristics from both RS and traction supply. The VAE successfully performs data embedding using only 16 channels in the latent space. The effectiveness of the method is quantified by means of the mean square reconstruction error (never larger than 1.5% and equal to 0.31% and 0.33% on average for the Swiss and French case, respectively). The t-SNE visualization confirms that overlapping of clusters is negligible, with a percentage of "misplaced" cluster points of 2.18% and 2.50%, again for the Swiss and French case, respectively. The computation time for the VAE prediction could be brought to some tens of ms representing a performance reference for future implementations. The proposed VI diagram assessment covers emissions for different OCs, rapid changes in power supply conditions, and background distortion caused by other trains on the same line, including line and impedance changes due to the moving load. In this perspective physical justification is found by domain knowledge integration for the identified clusters. A concluding discussion regarding advantages, limitations, and potential improvements or diversification is also included.

1. Introduction

The infrastructure of electrified railway systems (ERSs) is characterized by their complexity and disruptive importance in society, delivering a critical service for mass transportation. ERSs present wide use of static power conversion and feature dynamic load

☆ This work was supported in part by the Swedish Transport Administration.
* Corresponding author.
E-mail addresses: rafael.de.souza.salles@ltu.se (R.S. Salles), roger.oliveira@ltu.se (R.A. De Oliveira), sarah.ronnberg@ltu.se (S.K. Rönnberg), andrea.mariscotti@unige.it (A. Mariscotti).

https://doi.org/10.1016/j.compeleceng.2024.109730
Received 24 May 2024; Received in revised form 9 September 2024; Accepted 22 September 2024
Available online 30 September 2024

operation, making power quality (PQ) assessment complex, considering also the dependency between operating states and waveform distortion [1].

The range of manufacturers and technical solutions in railways further adds to this challenge, with different implementations depending on countries and historical factors. When considering distortion at harmonics and higher frequency, all systems are characterized by complex interaction between rolling stock (RS), fixed installations and traction supply line.

Assessing waveform distortion is necessary to evaluate and mitigate disturbance on internal and external systems, encompassing signaling and communications, power system protection and metering, and external communication circuits, as well as other railway systems. The lack of harmonized assessment approaches and the limitations of the established methods are pointed out in the literature, which creates an opportunity to develop alternative methods and propose new solutions [2,3].

Methods for modeling the interaction between RS and the traction power supply, including frequency-domain approaches and measurement-based models, have been investigated for ERS analysis regarding waveform distortion and systems resonances [4–8]. Data-driven models based on measurement analytics present a significant potential to provide information regarding waveform distortion characteristics and behavior, overcoming the limitations of traditional methods. Traditional PQ analysis approaches extensively used in distribution grids using aggregated 10-min values are not suitable for short-term variations, especially in ERSs, where operating conditions (OCs) can dynamically change the PQ parameters in a lapse of seconds. Characteristic patterns may be identified in relation to synchronous (harmonics) or non-synchronous (inter-harmonics) spectral components up to the whole 2 kHz to 150 kHz supraharmonic range.

Measurements of the pantograph electrical quantities are commonly recognized as the minimum informative set, as they are accessible, they describe the electrical interface with the traction supply network, and they are the quantities selected by the standards to discipline impact on the power supply and PQ [9,10]. Based on them, both the line and the RS impedance may be derived [7], as well as supply distortion and return current disturbance [11,12], all including variability for different supply conditions and RS OCs [13]. Considering power terms (active and non-active spectral components) and the impact of such components on the energy measurement accuracy and overall efficiency, some works provided insight on the influence of harmonic distortion and the uncertainty requirements for power harmonic terms [14,15]. The use of non-intrusive load monitoring (NILM) techniques to ERSs was explored [1], evaluating the informative content and the clustering performance of the two pantograph quantities (voltage and current), as well as the derived power and impedance quantities. Other applications of data-driven methods applied to ERS can then be found, such as machine learning distortion forecast [16] and low-frequency oscillation event detection [17].

Unsupervised learning combined with clustering can support waveform distortion assessment for railways through measured data dimension reduction. It was achieved in [1] with more classical techniques, such as principal component analysis and least-mean-squares regression, for characterization of RS OCs with VI diagrams and orthogonalized harmonic active and reactive power spectra. Pattern identification on clusters of the extracted features allows the interpretation of waveform distortion variations in different power system applications and architectures [18–20]. Patterns can be collected for harmonics, interharmonics, and supraharmonics, or even for the time-domain waveform in different time scales (e.g., 10-min, sub-10-min and sub-second values): a deep autoencoder (DAE) was applied to pantograph current measurements in [21], successfully correlating the RS emission with its operation. Deep clustering can thus be applied for PQ analysis in power systems by exploiting information in different domains.

Many works have applied deep learning (DL) for PQ analysis using classification or disturbance identification: classification algorithms are suitable for such tasks, having explored accuracy and potential for online monitoring applications [22–24]. Those methods are focused on segregating patterns through learning process algorithms based on labeled data (supervised). Non-labeled datasets (mostly PQ or waveform distortion measured data are unlabeled) are suitable for unsupervised learning, but not for supervised learning [25]. The unsupervised machine learning applications aim at finding patterns in PQ measurements, explaining the different behavior and variations, and combining domain knowledge integration for PQ assessment. Additionally, the literature (not limited to PQ analysis) demonstrates the success of unsupervised DL methods in feature extraction and pattern detection, overshadowing traditional machine learning performance [26]. Extended applications in other domain fields are diverse, using variational autoencoder (VAE) for instance, on latent feature representations to capture patterns in complex data, like target recognition on radar images [27], anomaly detection in the context of energy theft [28], hyper-spectral image classification [29], machine abnormal sound detection [26], fault diagnosis on machine vibration data [30], among others. Combining autoencoder-based techniques, clustering, and other architecture models, such as convolutional neural networks, long short-term memory networks, or transformer and graph networks, can provide suitable and advanced performance for the task in discussion.

This work proposes an automatic feature extraction based on 2-D time-domain representations using a VAE. The electrical quantities of interest are the pantograph voltage and current, represented by their VI diagrams (also known as “Lissajous curves”). For various OCs, patterns of waveform distortion are extracted. VI diagrams are provided to the VAE application as images for dimension reduction, and they are then subject to clustering with pattern inference. This work discusses cluster features with the objective of demonstrating the usability of inference information for waveform distortion assessment over the harmonics and supraharmonic frequency intervals. The methodology considers not only the RS characteristic emissions, but also the voltage supply conditions, since the VI diagrams represent the time-domain admittance at the pantograph (point of connection).

Two data sets are considered, related to two locomotives under different and distinct supply systems (the Swiss 15 kV 16.7 Hz system and the French 2×25 kV 50 Hz system), accompanied by information on OCs.

The main contributions and objectives of this work are listed below:

1. Discussion and demonstration of automatic feature extraction and pattern identification applied to VI diagrams represented as images, obtained from pantograph quantities in real conditions; these VI diagrams cover different OCs, rapid changes of power supply conditions, and background distortion, as caused by other trains on the same line, including line impedance changes due to the moving load.
2. Assessment and interpretation of such VI diagrams, quantifying the interaction between RS (source) and traction power supply (grid) for sub-second variations, which manages to include the complexities of ERS, and also explaining the patterns-based domain knowledge integration, associating the physical parameters of the system operation with the results.
3. Definition of a waveform distortion assessment and interpretation framework using unsupervised DL. Such a framework, as tested in the present application, can be then expanded to identify patterns in other applications for anomaly detection, harmonic analysis studies, and other PQ problems.

The remainder of the work is structured as follows. Section 2 provides a brief discussion on ERS distortion and the characteristics of VI diagrams of pantograph electrical quantities. Section 3 brings a description of the methodology used in this work, describing the pre-processing of input data, the deep VAE, clustering and inference. Section 4 reports the obtained results for the two different ERSs and a discussion of performance and applicability.

2. Waveform distortion and pantograph quantities

2.1. Waveform distortion in electrified railways

ERSs consist of one or more Traction Power Stations (TPSs) connected through overhead lines sections and transformers for delivery of power to moving loads (the trains). In AC ERSs power is distributed at the preferred fundamental frequency, corresponding to that of the national grid one (50 Hz, or 60 Hz in some countries), and a sub-multiple at 16.7 Hz in central Europe with the advantage at that time of lower line reactance and voltage drop. Operation of such infrastructure is traditionally ensured by the so-called Command and Control System, including safe circulation of trains. The electrical interaction among system elements (public grid, TPS, overhead lines, return current circuit, signaling system, RS, etc.) can be complex, and the dynamic power flow between TPS and RS, including regenerative braking, can impact line voltage stability or problems due to resonances [7,8]. In addition, interference to signaling circuits is a known relevant issue in normal and degraded modes [11,12]. Transients of various nature can represent both a source of additional interference and electrical safety issues caused by induction [31]. PQ compliance is a necessary condition in all scenarios for both DC and AC ERSs [32,33].

The extensive deployment of static converters, either on-board or at fixed installations, is the leading cause of harmonic distortion in railways [6,9,34]. Interharmonics are also expected due to the back-to-back conversion stages and the influence of the variable speed of locomotive power drives. ERSs are characterized by large power ratings of sources and loads, and still significant amounts of supraharmonic distortion were found in [21]. The presence of these components in the tens of kHz range represents a real risk caused by amplification due to line and return circuit resonances. Most wired control systems (e.g. signaling) operate up to about 20 kHz, overlapping to the harmonic and lower supraharmonic ranges, characterized by the largest distortion components.

These phenomena have their own characteristics, sources, effects, behavior, and challenges, as well as specific signal processing and quantification, necessitating a thorough comprehension of ERS generation and coupling mechanisms. Furthermore, waveform distortion and other PQ issues, in general, are the negative aspects of the operation of smart power solutions, oriented to improved performance and energy efficiency [35,36].

2.2. Lissajous (VI) diagrams for pantograph electrical quantities

Although electrical quantities in relation to distortion and interference are usually represented in the frequency domain, we will show that a time-domain waveform representation may highlight other characteristics providing some advantage. The VI diagram can show the waveshape behavior of different OCs of a power electronic load, including its interaction with the voltage supply. For RS those VI diagram will highlight visible changes between the various OCs, besides the change of orientation between acceleration and braking phases (due to the opposite power flow). Examples of VI diagrams during traction (red) and braking (green), of a commercial locomotive in a 15 kV 16.7 Hz system are shown in Fig. 1. The visual characterization of the elliptic form is noticeable for different explored OCs. Some aspects can be highlighted, like large spread for different power levels during traction, inverted angle in regenerative braking due to the reversed power flow, and some amount of distortion at standstill (no propulsion), due to the emissions of the auxiliary power converters.

This work uses the VI diagrams as data input for assessing waveform distortion parameters through a combination of DL and clustering techniques. The VI diagram shapes are transformed into images, where the elliptical patterns are taken from current plots versus voltage. Using images as inputs of the deep neural network allows the artificial intelligence (AI) models to automatically extract features related to the shapes. Such features at the end will contain the mapping of codes for pixel position variation that could be associated with parameters of the shape, such as inclination, area enclosed by the locus, line contour format, line intersections or self-intersections, and others, which are explored and explained in previous works [1,37,38]. Those generated images have a reduced size to comply with the computation burden of training and prediction of the AI model. A pixel resolution of 320×400 is defined empirically to guarantee reliable results. The processing of those input data is further defined in the following section.

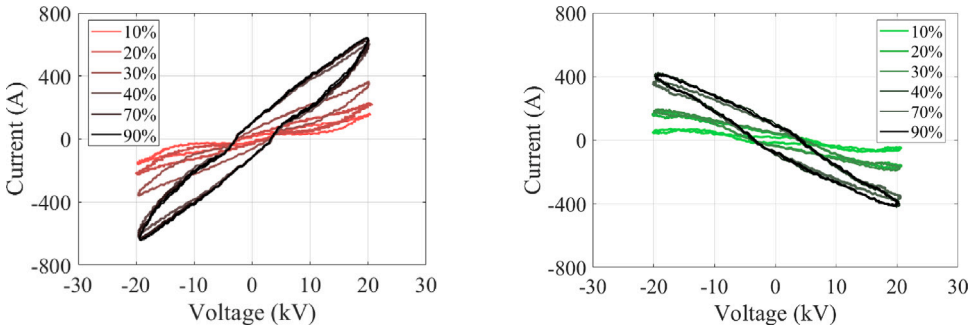

Fig. 1. VI diagrams at various percentages of absorbed current measured with respect to the nominal value of the Swiss locomotive Re460: traction (left), braking (right).

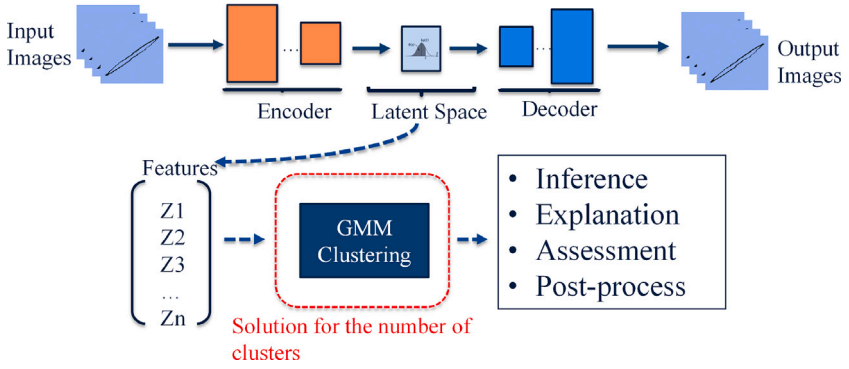

Fig. 2. Schematics of the proposed method.

3. The proposed methodology

The proposed method is based on dimension reduction and clustering of the VI diagrams of the measured pantograph quantities. Autoencoder-based DL techniques have been proven to be a good option for automatic feature extraction of high-dimensional data, unlike traditional machine learning methods [25,26]. The technique applied to the present case aims to automatically extract the features by encoding and decoding the VI diagram images using VAE. A semi-supervised clustering based on the Gaussian mixture model (GMM) is then performed [39], and data separation is handled in an unsupervised way. The number of clusters is determined by visualization of clustered data, and t-distributed stochastic neighbor embedding (t-SNE) evaluation [40]. Fig. 2 illustrates the methodology that combines automatic feature extraction of VI diagrams and pattern identification using clustering for further analysis and inference.

The choice of using images as data input in this approach is to explore the potential of image-oriented methods. These methods are suitable for evaluating the VI trajectory characteristics that are recurrently discussed in this work. Noting the risk for unnecessary computational effort due to the larger dimensions and significant empty background of the images, using instead the VI information directly in some encoder-based or other types of machine learning method is more complicated than it seems. It involves time-domain admittance and complex numbers, necessitating the use of more advanced techniques and solutions for training and clustering features, not excluding an increase of the apparently reduced computational effort.

3.1. Input pre-processing

The input data are the VI diagrams generated by plotting a 5-cycle voltage waveform for the x-axis and a 5-cycle current waveform for the y-axis, as available in [41]. Each plotted VI locus is saved as a gray scale image, then binarized (i.e. thresholded) and reversed, with VI trajectories receiving logical value 1 (white color) on a black background. The input size is set for 320 × 400 2-D images. Fig. 3 illustrates the workflow of the pre-processing of input data.

As mentioned in Section 2.2, the shape of the VI diagram, called “trajectory”, can carry information regarding time-domain admittance at the measurement point, and those parameters associated with this wave shape of current and voltage must be captured in detail. This shape information will be of significant importance in the training process of the VAE, the visualization of results, and extracted features patterns. Back-and-forth resizing can compromise those aspects and smaller dimensions will deteriorate the image details necessary for the waveform distortion analysis proposed in this work. Fig. 4 illustrates the different sizes of a VI image and the clear visualization of details lost. From this reasoning, to avoid discontinuity of the trajectory or missing informative pixels, the 320 × 400 size was identified as the best choice for these data in particular.

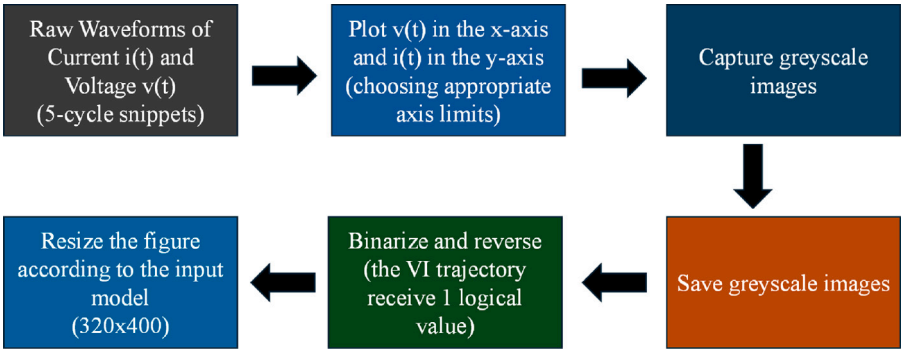

Fig. 3. Data input pre-processing workflow.

Fig. 4. Same image put with different sizes for observing lost on details: 320 × 400 (left), 160 × 200 (center), 80 × 100 (right).

3.2. Deep variational autoencoder

The autoencoder architecture is a leading algorithm in deep unsupervised learning, which during the training process ensures the minimum reconstruction error between encoder input and decoder output, executing a dimension reduction in the hidden layers of the network [42]. This reduction can be interpreted or explored as the selection of the strong features of the input data, called "latent space". Those features can be used for clustering problems, anomaly detection, automatic feature extraction to support other machine learning problems, image processing, or any other solution that requires dimensionality reduction.

The main difference between VAE and traditional autoencoders is the imposition of a prior distribution $p(z)$ on the latent space z, where the latent parameters are described in probabilistic terms, characterized by mean μ and dispersion σ [43]. From μ and σ, the final latent space is then sampled by $z = \mu + \sigma \times \epsilon$, where ϵ is a random variable drawn from a normal distribution $N(0, I)$, where I is the identity matrix [44]. The model optimizes the variational inference objective by applying stochastic gradient descent and standard backpropagation. The process results in a distribution over the latent code, avoiding empty spaces [42].

Also, modeling this variance into the latent space represents an advantage of the VAE. This property allows specific sensitivity to reconstruction by varying the variance. In other words, the VAE can capture the slight variations of an input set without segregating it as a different input type, and it is pretty helpful for image analysis [45]. For instance, it is common for hand-writing image assessment to have inputs of the same "letter" or "number" that can be written differently. This fact can be related to the problem explored in this work, where slight changes can happen within the same group of VI diagrams due to voltage supply conditions and the moving load. One should be able to differentiate whether there is a substantial change in waveform distortion pattern and also capture variability within the OCs.

From this point, each element x_n from the input data $X_n = x_1, x_2, \ldots, x_n$ can be generated from z under the prior distribution $p(z)$ and the network optimized parameters. The objective function of the training parameters is described in the reconstruction loss measured as mean square error (MSE) (1), Kullback–Leibler divergence (KL_{loss}) (2), or the evidence lower bound (ELBO) loss (3).

The reconstruction loss measures the difference between the encoder input X_n and the decoder output Y_n using a MSE error metric (MSE_{loss}). The KL_{loss} measures the difference between two probability distributions, ensuring that the learned means and variances are as close as possible to the normal distribution, for a latent space with d dimension, with n the number of input samples and i the interactive observations. The equation provided for KL_{loss} is a simplified and specific form of the KL divergence used on VAE training, where it is assumed that the both posterior and the prior are Gaussian distributions. The VAE architecture and training algorithm are more extensively discussed and evaluated in [44,46].

$$MSE_{loss} = \frac{1}{n}\sum_{i=1}^{n}(Y_i - X_i)^2 \tag{1}$$

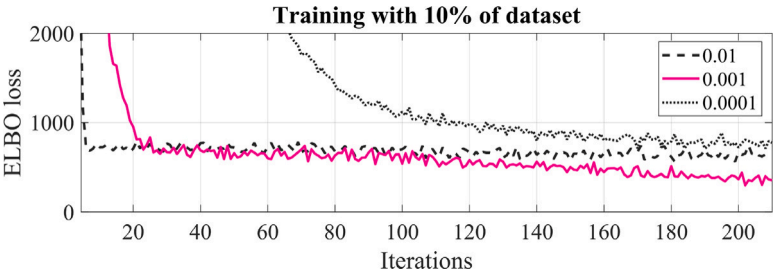

Fig. 5. Preliminary test of learning rate (ranging between 0.0001 and 0.001) with 10% of the training dataset.

Table 1
Proposed VAE parameters.

Layer	Type	Size	Number of filters
Input	Input	[320 400 1]	–
Encoder	Convolution + ReLU	[3 3]	32
Encoder	Convolution + ReLU	[3 3]	64
Encoder	Fully Connected	32	–
Encoder	Sampling Layer	16	–
Decoder	Projection and Reshape	[8 100 64]	–
Decoder	Transposed Convolution + ReLU	[3 3]	64
Decoder	Transposed Convolution + ReLU	[3 3]	32
Decoder	Transposed Convolution + ReLU	[3 3]	1
Output	Sigmoid	–	–

$$KL_{loss} = -\frac{1}{2}\sum_{i=1}^{d}(1 + \log(\sigma_i^2) - \mu_i^2 - \sigma_i^2) \tag{2}$$

$$ELBO_{loss} = MSE_{loss} + KL_{loss} \tag{3}$$

The architecture and input information used in this work are described in Table 1, where the number of latent channels proposed is 16. The "Sampling Layer" predicts the z, μ, σ, for a given input, and the "Project and Reshape Layer" reshapes the given latent space to the decoder convolution again. The training hyperparameters are as follows: 30 epochs, mini-batch-size of 64, learning rate of 0.001 (the one that offered smaller losses and reasonable fast convergence).

This architecture and its hyperparameters were a trade-off between creating a bottleneck to favor dimensional reduction, and achieving a significant small reconstruction error and fast convergence. The initial choice of the architecture was mostly inspired by previous works that use auto-encoder architecture [19,21]; after some trial-and-error attempts the hyperparameters values shown in Table 1 were obtained. Fig. 5 shows an example of a preliminary test of learning rate with 10% of the training dataset. The computational complexity of the models described in Table 1 amounts to 510.7 millions of floating point operations, or MFLOPs [47].

3.3. Clustering

GMM clustering is applied to the extracted features by the VAE model to assess the patterns of the input. A GMM assigns posterior probabilities to multivariate normally distributed components and performs hard clustering by selecting the component with the highest probability for the assigned cluster for a given observation [48]. It assumes that the instances were generated from a mixture of several Gaussian distributions, whose parameters are unknown, and all instances generated from a single Gaussian distribution form a cluster that typically looks like an ellipsoid [49].

GMM clusters requires a prior choice of the number of clusters, and Fig. 6 shows the scheme for this choice during the clustering process. GMM is chosen over other simpler techniques, as k-means, for better handling of the Gaussian noise generated in the VAE features. It has the following advantages:

- each data point has a likelihood affiliation with any given cluster, instead of a hard deterministic assignment;
- utilization of three key parameters (number of clusters, cluster mean and cluster covariance);
- utilization of all data points in the dataset to update the cluster parameters;
- addressing the 'circular' distance around the centroid in its embedded calculation and utilization of the covariance matrix, while other simple methods like k-means require feature standardization [44,50,51].

The number of clusters k is found with "trial and error" analysis, where k starts from 2 and is incremented until a reliable data separation is found. This is verified by means of t-SNE [40], and using visualization and interpretation of the image cluster population.

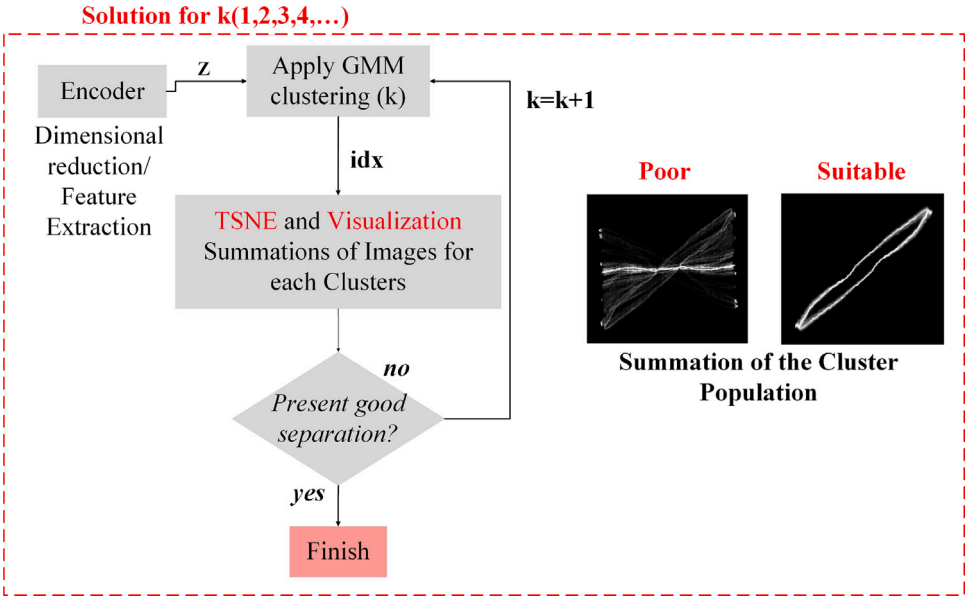

Fig. 6. Number of cluster choice based on TSNE and visualization.

The GMM algorithm handles a set of Gaussian distributions of mean μ_k and dispersion σ_k, where k is the number of clusters, and there is also a fraction of data points called density π_k [52]. Three steps describe the algorithm [39,52]: during estimation, the probability is calculated for each data point f_i belonging to each cluster and the assigned point n_k and distribution in (4); a data point f_i is assigned to cluster k taking the largest $r_{(i,k)}$ value; and during the maximization step, parameters are updated, calculating π_k as the fraction of data points effectively assigned to cluster k, as described in (5) and (6).

$$r_{i,k} = \frac{P_b\{f_i \in k^*\}}{\sum P_b\{f_i \notin k^*\}} = \frac{\pi_{k^*} N(\mu_{k^*}, \sigma_{k^*})}{\sum_{k \neq k^*} \pi_k N(\mu_k, \sigma_k)} \tag{4}$$

$$\pi_{k^*} = \frac{n_{k^*}}{\sum_1^k n_k} \tag{5}$$

$$\mu_{k^*} = \frac{\sum_i r_{i,k^*} f_i}{n_{k^*}}, \pi_{k^*} = \frac{\sum_i r_{i,k^*} (f_i - \mu_{k^*})'(f_i - \mu_{k^*})}{n_{k^*}} \tag{6}$$

3.4. Inference and clusters assessment

After the clusters are defined, parameters are quantified to assess and validate the VI diagram patterns found by the DL method. This part of the work aims to explain and make inferences about the resulting clusters, extending to a waveform distortion assessment framework for VI diagrams. The following quantifications and visualizations are proposed in this work:

1. Assessment of the OC of each cluster by plotting colored fundamental current data points in polar plots. In this way the OCs will be highlighted by the amplitude and direction of the locomotive absorbed current.
2. Spectra patterns based on the mean value of parameters for each cluster: harmonic spectra and 200 Hz bands grouping supraharmonic spectra. The computation adapts the IEC 61000-4-7 [53] for 5 cycles measurement interval (DFT resolution is 10/3 Hz for the 16.7 Hz data and 10 Hz for the 50 Hz data). The supraharmonics grouping goes up to 20 kHz for both datasets explored in this work.

In this way, one can identify the characteristic RS emission for traction or braking operation within several stances of absorbed power. Also, the variations in the power supply and locomotive interaction can be assessed by comparing current and voltage spectra, looking into discrepancies in the voltage supply conditions and impedance change due to the moving aspects of the load.

4. Results

In this study case, the methodology is applied to pantograph current and voltage measurements from two different locations and locomotives. The dataset [41] contains recordings of pantograph electrical quantities from Switzerland and France. The supply system for the Swiss line is a 15 kV 16.7 Hz, operating a Re460 commercial locomotive with a rated power of 5.6 MW. The supply system for the French line is a 2 × 25 kV 50 Hz, operating a TGV Dasye EMU dedicated for the test with 9.28 MW rated power. As

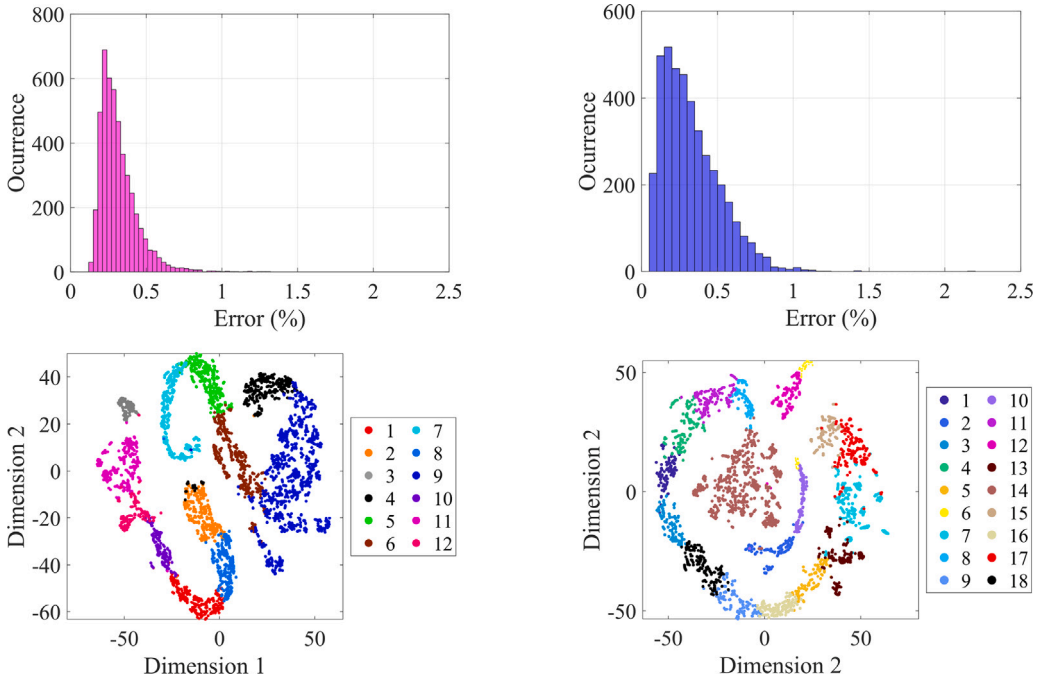

Fig. 7. Distribution of MSE reconstruction error between DAE input and output (top) and t-SNE criterion results (bottom) for Switzerland data (left) and France data (right).

described in [41], the pantograph measurements are organized in waveforms of 300 ms and 100 ms duration, for Switzerland and France, respectively, sampled at 50 kHz. The dataset also contains information regarding other variables describing the OCs, like overall rms RS current, speed and OC label. The study case, at this point, aims to cluster the VI diagrams from 5-cycle voltage and current waveforms (4683 and 4124 input samples, for Switzerland and France measurements, respectively). For this work, only acceleration and braking states were included in the analysis.

The deep clustering application to both railway systems showed a small reconstruction error, evaluated by MSE, after the VAE training, as illustrated in Fig. 7 (top), for the Swiss and French measurements. The input data were assigned with 12 clusters for Switzerland and 18 for France. The t-SNE results illustrate the cluster separation in a two-dimensional representation, as shown in Fig. 7 (bottom). The MSE error in average values, is 0.31% AND 0.33%, for the Swiss and French case, respectively. The clustering separation has shown to be suitable and the t-SNE visualization and analysis of the image separation can confirm it. The VI diagrams in the same cluster present a likeness or resemblance in shape. In addition, the clusters overlap coefficient, extracted from t-SNE curves, for the Swiss and French cases is 2.18% and 2.50%, respectively.

In addition, the VAE model prediction times were computed, resulting in mean values of 12.5 ms for encoding and 117 ms for decoding (performed on MATLAB R2022a, and hardware as follows: x64-based PC, 11th Gen Intel(R) Core (TM) i7-1165G7 @ 280 GHz, 2803 MHz, 4 Core(s)). It must be underlined that such figures are a significant overestimation, since function calls in MATLAB are so slow that is impossible to really estimate the real computation effort of the calculations alone, and likely those times can be decreased out significantly in C or Python, such as by at least one order of magnitude [54].

Fig. 8 shows the overlapped images for each cluster for each of the two systems. Looking at the cluster separation, it is possible to identify different shapes that can be associated with changes in operation and characteristic interaction between RS and railway power supply. For instance, the opposite sign of current waveform due to regenerative braking is expected, producing negative slopes during braking operation, which is also identified by the method.

In the following inferences can be combined regarding waveform distortion, RS operation, and the interaction between the distortion source and grid through the time domain variation of the distortion components and admittance. The results aim to cover clusters from different OCs and the same operation, but with variations in distortion.

4.1. Switzerland measurement results

Evaluating the results for the Switzerland measurements, it is possible to assess inference about cluster information according to the OCs and waveform distortion. Clusters 1, 2, 3, 4, 8, 9, 10, 11, and 12 belong to the traction condition of the locomotive, while clusters 5, 6, and 7 present the braking OC signature.

That visualization can be done by looking into the VI diagram slopes, as explained before, but also from the engineering knowledge of railway systems. To validate and provide more information, Fig. 9 shows the polar plot of the fundamental frequency

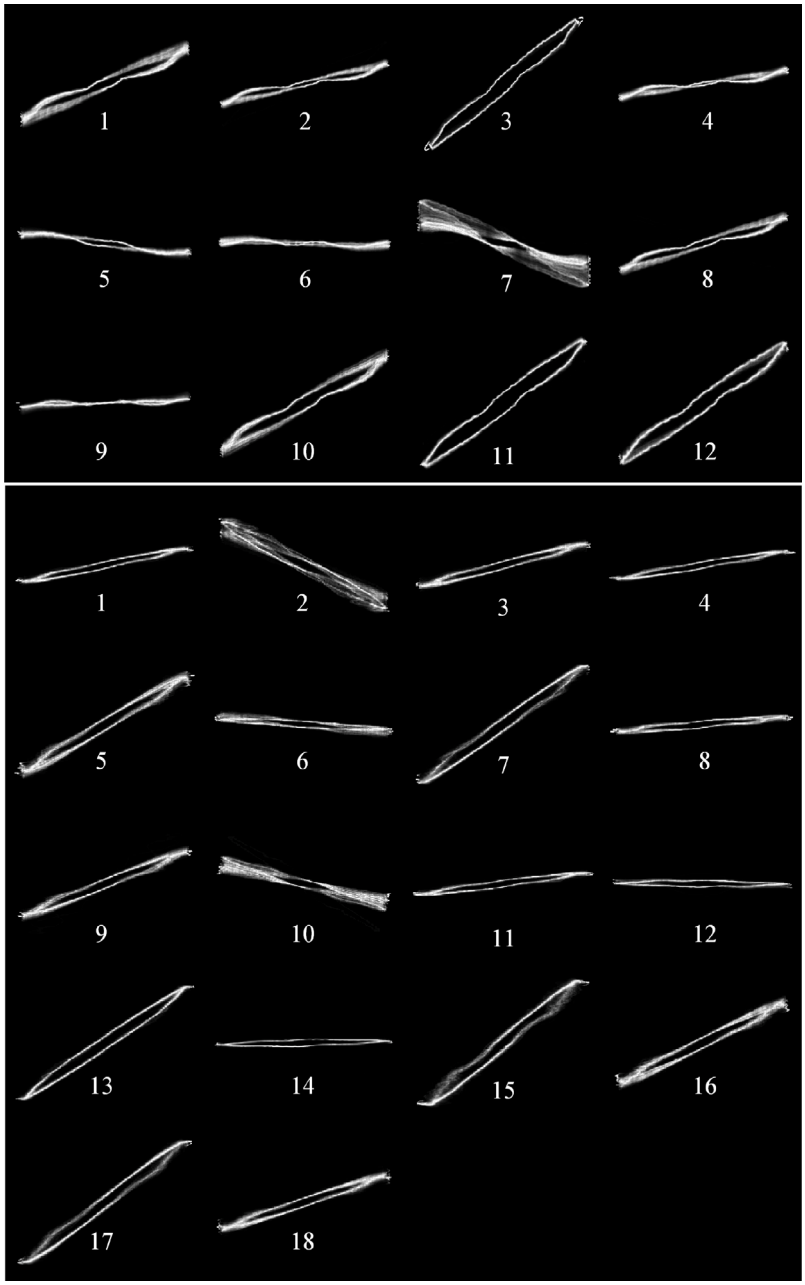

Fig. 8. Overlapping of images of each cluster for Switzerland data (top), and France data (bottom).

of the pantograph current. It is possible that the clusters also present signatures for different OCs and according to the current amplitude, which is correlated to the RS absorbed current or power. For traction, cluster 9 represents the fundamental current up to around 50 A, cluster 4 represents values between 50 A and 100 A, clusters 2 and 8 values between 100 A and 200 A, cluster 1 with values between 200 A and 275 A, and clusters 3, 10, 11 and 12 with values up to 425 A. For braking, an opposite angle is observed due to the regenerative current flow, cluster 6 ranging up to 50 A, cluster 5 with values between 50 A and 100 A, and cluster 7 between 100 A and 300 A.

Regarding waveform distortion, for harmonics and supraharmonics, different emission signatures can be expected among the clusters due to changing OCs or changes in the grid power supply as resonances and background distortion.

Fig. 10 shows the harmonic and supraharmonic spectra for clusters 3, 11, and 12 of current and voltage, representing full traction operation. The onboard converter signature emission is visible in the 666 Hz to 966 Hz band (lateral bands located at harmonics of order 40 and 60, that are symmetric around 800 Hz) and 1333 Hz to 2000 Hz in the harmonic current spectra. Still, cluster 12 spotted

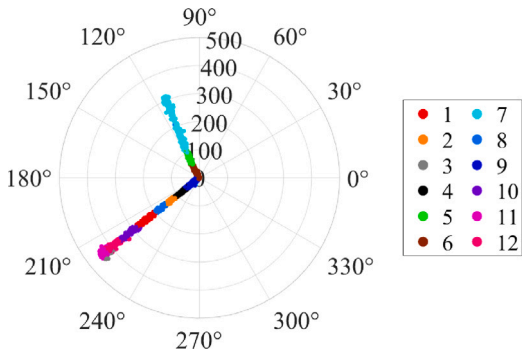

Fig. 9. Fundamental frequency (16.7 Hz, Switzerland) polar plot by sample and cluster color.

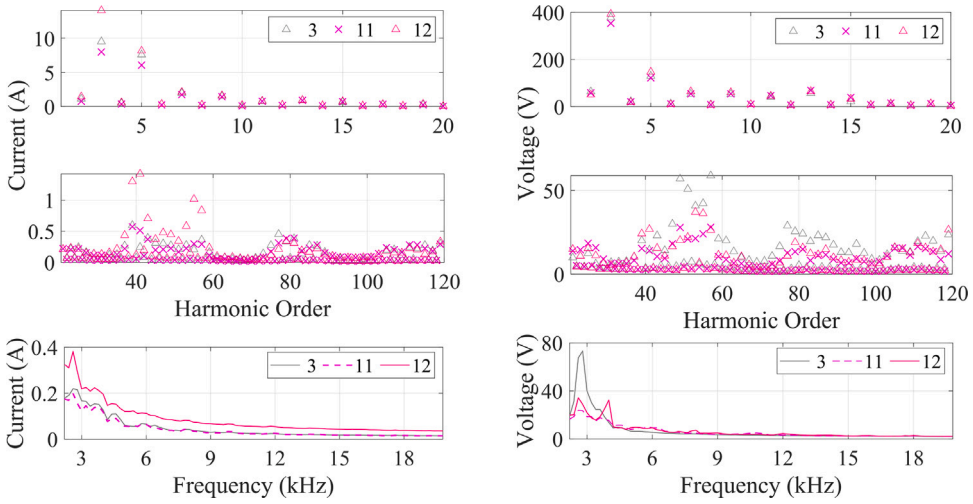

Fig. 10. Spectra patterns for cluster, 3, 11 and 12 of Switzerland data (16.7 Hz fundamental): harmonics current (top left), harmonic voltage (top right), supraharmonic current (bottom left), and supraharmonic voltage (bottom right).

higher mean values for the lateral band frequencies, with amplitudes above 0.75 A, while clusters 3 and 11 present similar spectral components to each other. The third harmonic shows variations according to the group, with mean values of 15 A, 10 A, and 8 A for clusters 12, 3, and 11, respectively. The third harmonic varies with higher dependence on the operation and the absorbed RMS current. However, clusters 11 and 3 have a higher amplitude of the fundamental according to the polar plot, which can indicate some change in the emission for cluster 12. Looking at the current at the supraharmonic range, cluster 12 also presents higher amplitudes and peaks compared to the other two clusters.

The method also captures signatures from the voltage spectra, showing similar emission can present distinct effects on the pantograph voltage, as observed for cluster 3, which present mean values spectra with higher amplitude around the switching frequencies and between 2 kHz and 3 kHz. That happens due to the interaction between the disturbance source, RS emission, and the traction power supply impedance, indicating a larger line impedance in that interval.

Considering the harmonic or supraharmonic impedance Z_h estimated as $Z_h = V_h/I_h$ over the harmonic and SH frequency intervals, one can observe that the impedance estimate for cluster 3 is around 320 Ω taken at 2.6 kHz for example, while cluster 11 shows 120 Ω and cluster 12 shows 90 Ω at the same frequency. This example also highlights that even with similar shapes and images, details of the VI diagram with high-frequency components can differentiate the patterns.

Fig. 11 illustrates another example of the Switzerland measurements, now exploring the difference between braking and traction operations, considering clusters 5 and 7 for the braking, and clusters 11 and 12 for the traction OCs. The results show slight differences for the third and fifth harmonic of the current, although the two pairs of clusters are not clearly separated (Fig. 11 top left). The switching frequency signature between 666 Hz and 966 Hz (harmonics 40 and 58) is evident for both current and voltage (the voltage being excited by the line impedance reaching a non-negligible value at such frequency). Also at the 2nd harmonic group of the switching components (between about harmonic orders of 80 and 116) some dispersion is visible. For harmonic voltage spectra those clusters did not show appreciable differences.

Considering the supraharmonic spectra shown in the lower part of Fig. 11, the low frequency portion reflects what already observed in the harmonic spectra, but at broader frequency resolution: the two peaks in the voltage spectrum correspond to the

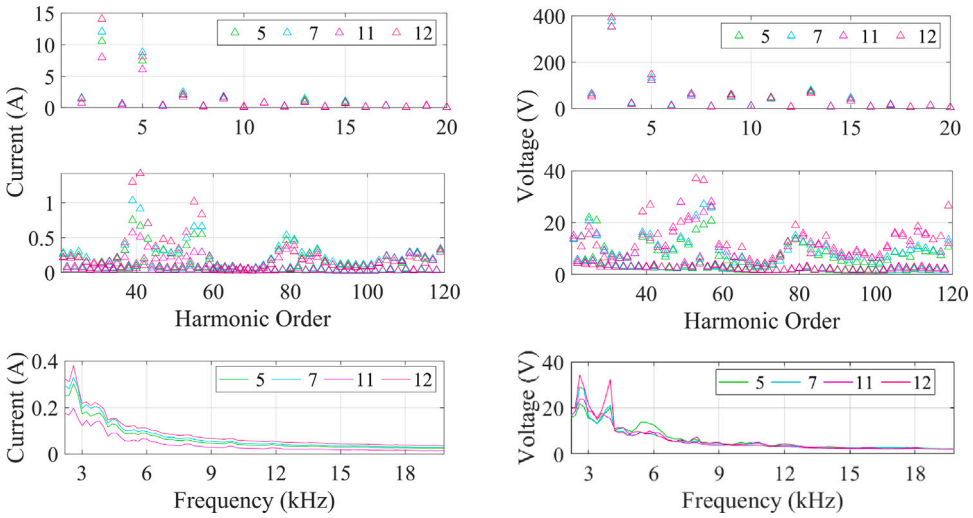

Fig. 11. Spectra patterns for clusters 5, 7, 11 and 12 of Switzerland data (16.7 Hz fundamental): harmonics current (top left), harmonic voltage (top right), supraharmonic current (bottom left), and supraharmonic voltage (bottom right).

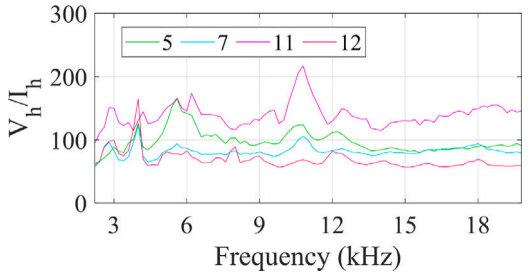

Fig. 12. Impedance spectra result considering the V_h/I_h ratio for the Swiss case.

2nd group of the switching components (at about harmonic orders 80 and 116), the lower one "integrated" by the peak occurring between components of order 40 and 58, almost corresponding to a single component in the SH range representation. Around 3.8 kHz to 4 kHz the two clusters for braking show a remarkable difference in voltage. The SH groups for current are instead not so diversified and the two braking clusters are always bracketed by those of the traction OC.

It may be observed that the two clusters for the braking OC have lower Z_h values: selecting again 2.6 kHz, cluster 5 presents around 70 Ω and cluster 7 about 90 Ω, while cluster 12 also about 90 Ω and cluster 11 up to about 120 Ω. It seems that changes in the high-frequency impedance are a good indicator to differentiate the patterns identified by the method within similar OCs.

Fig. 12 illustrates an example of visualizing the different Z_h values for the 4 selected clusters.

4.2. France measurement results

Considering the results for the France measurements, we may distinguish a large set of clusters (1, 3, 4, 5, 7, 8, 9, 11, 13, 14, 15, 16, 17, and 18) belonging to the traction OC of the locomotive, whereas fewer (clusters 2, 6, 10, and 12) present the braking OC signature. Analogously to the Switzerland case, Fig. 13 shows the polar plot of the fundamental of the pantograph current distinguishing the various clusters, with obvious location of those in traction and braking OCs.

Regarding the larger number of clusters under the traction OC, there may be various explanations that are centered around the fact that the traction OC lasts for longer time intervals than the braking OC: during such intervals, it is thus more likely that the supply conditions change. It is also simply possible that the harmonic behavior is more variable due to more complex interactions with the traction inverters, as this type of train has a more direct connection between the traction line and the traction inverters through simple rectifiers, rather than four-quadrant converters, as in the Swiss locomotive.

Clusters 14, 8, 11, and 3 captured traction conditions up to 200 A, while clusters 18, 9, 16, and 5 conditions up to 400 A. The full traction conditions, with values between 400 A and 500 A, were observed for clusters 7, 13, 15, and 17. For braking operation, cluster 6 and cluster 10 have VI diagrams with fundamental current values up to 200 A and cluster 2 shows OCs between 200 A and 400 A. Cluster 12 is also from braking OC, but has a significantly low current value, similar to cluster 14 for the traction OC.

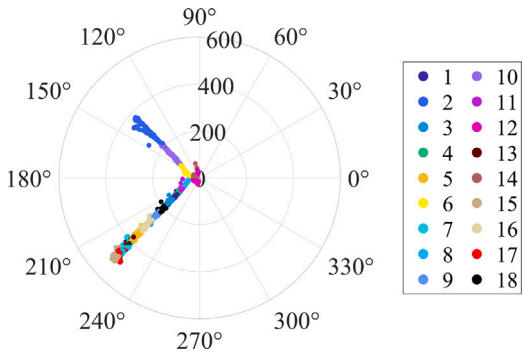

Fig. 13. Fundamental frequency (50 Hz, France) polar plot by sample and cluster color.

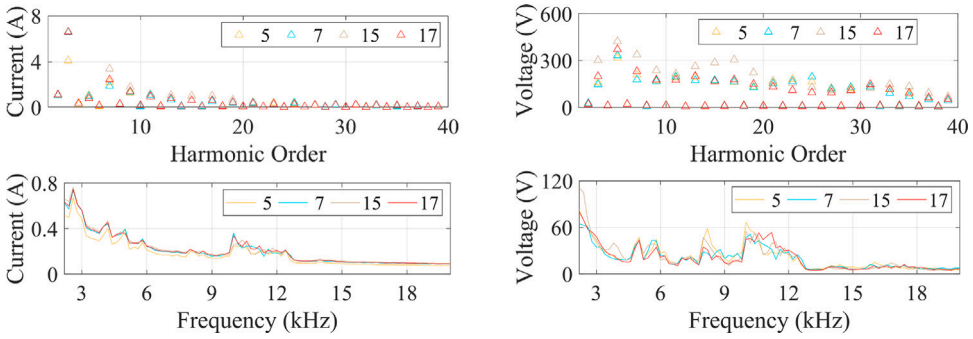

Fig. 14. Spectra patterns for clusters 5, 7, 15 and 17 of France data (50 Hz fundamental): harmonics current (top left), harmonic voltage (top right), supraharmonic current (bottom left), and supraharmonic voltage (bottom right).

The information from the cluster-based analysis is complemented by the assessment of waveform distortion. Fig. 14 shows harmonic and supraharmonic spectra of pantograph voltage and current to compare clusters from traction OCs above 300 A of fundamental current intensity (clusters 5, 7, 15, and 17). The third harmonic presents higher amplitudes compared to other low-order harmonics, around 7 A, except for cluster 5, which is in an instance before full traction operation, below 400 A of fundamental. All clusters present low amplitudes of fifth harmonic. Some onboard featured emissions can be observed in the supraharmonic range: narrow-band emission from 2 kHz up to 6 kHz and broadband emissions from 10 kHz to 12.4 kHz. For the supraharmonic range, it is possible to observe that the higher the power operating point of the locomotive, the higher the amplitude of the distortion.

There are waveform distortion dissimilarities in the voltage spectra, where high-order and low-order harmonics present different levels among the clusters, indicating the influence of the voltage power supply conditions. In the supraharmonic range, cluster 5 presents some signature distortion at 3.8 kHz, not present in other clusters. Also between 10 kHz and 12.4 kHz, different voltage amplitudes appear at characteristic frequencies, like 10 kHz, whereas for cluster 5 and 7 the voltage component is 20 V higher for cluster 5 and has emission of 0.1 A lower than cluster 7. Looking at the estimated impedance Z_h, this scenario indicates 256 Ω for cluster 5 and 130 Ω for cluster 7 at 10 kHz. Clusters within similar traction OCs present different impedance for higher frequencies, also for the French case. Thus, it is also possible to distinguish between clusters of the same fundamental intensity by examining the high-frequency impedance.

Fig. 15 shows the results of French measurements comparing braking conditions (clusters 2 and 10) with full traction (cluster 15). It is interesting to observe that the emission levels are higher for full traction OCs compared to braking conditions, which can be observed for the low-order harmonics and the supraharmonic range, with the exception of the interval between 10 kHz and 12.4 kHz where the emission is quite similar for all clusters. For the third harmonic, the mean values of cluster 15 show distortion around 7 A, while the clusters from braking show distortion below 4 A. Also considering the impedance Z_h in the SH range, the differences between patters becomes more evident. For instance, at 3.6 kHz there are higher impedance values for the braking conditions, with 220 Ω for cluster 2, 495 Ω for cluster 10, compared to 79 Ω for cluster 15. The same can be observed looking at other frequencies around the spectra, such as 8.8 kHz, 11.8 kHz, 16 kHz, etc. Fig. 16 illustrates another example of the France case for visualizing the different impedance results.

4.3. Discussion

The method is suitable and efficient in finding patterns using VI trajectories. The VI locus features are extracted automatically, and clustering captures the pattern information regarding OCs and distortion. Some more detailed considerations are provided below.

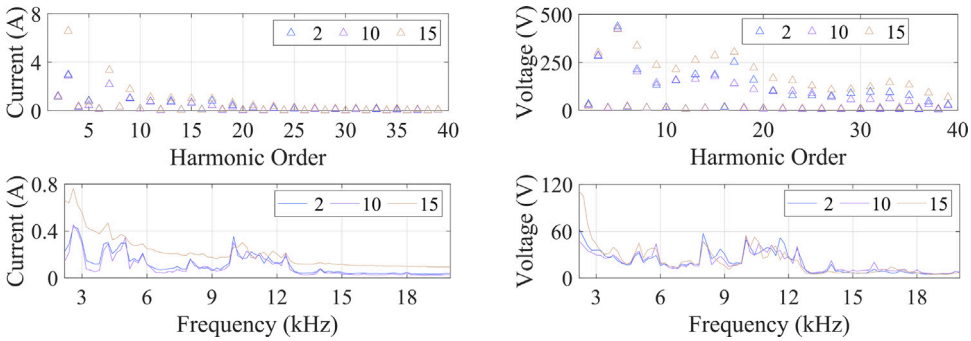

Fig. 15. Spectra patterns for clusters 2, 10 and 15 of France data (50 Hz fundamental): harmonics current (top left), harmonic voltage (top right), supraharmonic current (bottom left), and supraharmonic voltage (bottom right).

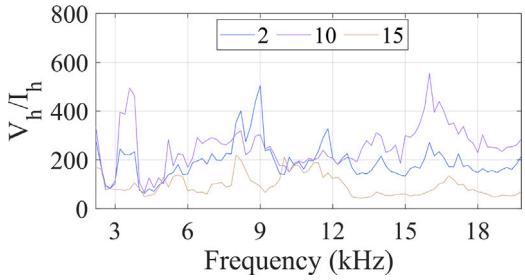

Fig. 16. Impedance spectra result considering the V_h/I_h ratio for the French case.

1. The proposed method, which automatically extracts features from VI diagrams, can find patterns for both OCs and distortion, making it possible to create inferences and explanations about the two aspects. A variation in the conditions of the distortion components was identified for sub-second variation in the time domain, which is also true for the voltage supply conditions and interactions between RS and railway grid, capturing changes in impedance as well. It represents the major advantage of using VI diagrams as input, since it comprises all information in one representation, considering the time-frequency behavior. Traditional PQ analysis methods based on pure frequency domain analysis can lead to wrong or limited interpretations of ERPS's dynamic and complex behavior.
2. The results highlight the advantage of using automatic feature extraction and deep clustering technique on VI diagram images, which are 2-D representations, for PQ analysis. Additionally, this work presents a simple framework that combines techniques and engineering knowledge to choose the number of clusters in a semi-supervised way, allowing the choice based on the valuable information to be extracted from each group, which is not highly time-consuming. Those target inferences can be used to support pre-assessment for modeling harmonic sources, anomaly detection, or other PQ events identification.
3. The proposed framework is based on the offline VAE and GMM clustering application. The assessment requires domain knowledge integration, where the number of clusters is semi-supervised. The analysis of the waveform distortion parameters depends on the expert knowledge of the spectra content, OCs, and studied railway installation. The post-processing procedure is not fixed and can vary depending on the analyzed subject. However, the DL methodology, requiring detailed knowledge, can be applied similarly across various PQ data analyses within power systems. Offline applications are appropriate for evaluating power systems performance, investigating and characterization problems, and diagnosing systems without needing a fast report or results [55].
4. Using VI diagrams for pattern recognition of 2D image-like representations involving two quantities simultaneously, whose together additionally get impedance information from the shape, proved adequate for waveform distortion assessment for RSs using the proposed methodology. Additionally, future approaches could combine the achieved contributions of this work for application on power terms measurement data from railways. The significance of active and reactive power spectra in pattern identification for railway applications demonstrated before [1,15] can further underscore the potential of our approach. Future works can potentially enhance the methodology by exploring using time-domain objects to represent power terms as VI diagrams.
5. Cluster algorithms like GMM and k-means use a pre-determined number of clusters as parameter for convergence. In this work, the number of the clusters used for input of the GMM algorithm was defined in a semi-supervised way, where a process that combines visualization techniques helps finding a suitable solution. However, it can represent a disadvantage for larger and more complex datasets that have not so well-defined cluster shapes. Alternatively, density-based clustering techniques can be a solution in the future. These techniques infer the number of clusters based on the data, and they can discover clusters

of arbitrary shape (e.g., density-based spatial clustering of applications with noise, known as DBSCAN [56], or kernel density estimator, known as KDE [57]), potentially opening up new possibilities for the proposed method.

6. Dimensional reduction methods are abundant in machine learning and deep learning. The choice for a specific method will depend mainly on the input data characteristics (e.g., dimensionality, variability, amount of data, etc.), and the type of post-processing analysis. The advantages of deep learning methods based on autoencoder are highlighted by this work. Still, other techniques have the potential for suitable performance within the proposed framework, as diffusion probabilistic models. Diffusion models, with a special mention for denoising diffusion probabilistic models (DDPMs), are a branch of probabilistic generative models that iteratively ruin data, adding noise [58], and by reversing this process learn data embedding. This process is done by two back-and-forward Markov chains, where the main first objective is to take any data in a simple distribution, and the second stage uses deep learning to learn transition kernels [58,59]. However, the application of this method is relatively new and mainly focuses on data or image generation, language programming, computer vision, and temporal data modeling [58]. Time for maturity and method adjustment are necessary for it to apply to PQ studies.

The considerations above highlight that the results and the established framework provide an alternative to waveform distortion assessment in ERS studies compared to traditional PQ analysis, with the possibility of expanding to other applications that involve pattern identification within complex data, such as systems with renewables, power drives and significant amount of static power conversion. The methodology makes it possible to make inferences on the time-varying behavior of moving loads interacting with the railway power supply, validated with two different systems that present their challenges with peculiar arrangements and particularities of the power delivery scheme. Additionally, future works can benefit from this framework for exploring other parameters associated with waveform distortion and using adapted similar techniques to optimize inference and execution.

4.4. Verification against other parameters with physical meaning

The reported results have shown the patterns characteristic of harmonic and supraharmonic distortion and their association with OCs. Besides major and more evident parameters covered by the VI trajectory, the shape is characterized also by other details of the voltage and current conditions at the measurement point (as introduced in Section 2.2 and discussed in [1]). To illustrate that the extracted feature patterns are associated with those details bearing physical meaning, Fig. 17 shows some time-varying distribution of those parameters that are separately calculate with the cluster results. In order to save space, this discussion will focus on the Switzerland case only.

The maximum voltage parameter $V_{\max}$ (Fig. 17, top left) is extracted as the peak value of the voltage waveform of each VI diagram: it does not contain information on the RS operation, but rather on the line supply conditions. It may be seen that cluster 12 represent a similar OC as cluster 11, but separates the underlying supply voltage behavior with the voltage drop possibly caused by a line impedance change due to the distance from the TPS or by power absorption of nearby trains. The method thus identifies the change in the boundary condition that would be detected by separately calculating the $V_{\max}$ parameter.

The area A of the enclosed locus within the normalized VI trajectory (Fig. 17, top right) describes at the same time current intensity and loop aperture; the latter will indicate the degree of phase difference between the pantograph quantities. Also, the sign of the area will indicate the direction of the loop (clockwise for positive, anti-clockwise for negative). The current span between two extremes $I_{\min}$ and $I_{\max}$ [1] (shown in Fig. 17, bottom left) correlates with the fundamental active power.

The slope angle ξ of the line joining current extremes is another parameter distinguishing direct and reverse power flow, calculated as the arc angle produced by the change in current divided by the change in voltage between the points of maximum and minimum current. Also this parameter is directly dependent on the current variation, since we may say that there are no significant changes in voltage without external disturbances. The angle ξ is a measure of the fundamental admittance and it can be tracked for changes between OCs. Its behavior is shown in Fig. 17, bottom right, highlighting very well the arrangement of the clusters in horizontal stripes; such strong correlation may be led back to the change of slope with increasing current shown in Fig. 1.

Regenerative braking explains negative slope and clockwise trajectory values rather than being due to capacitive behavior (as also highlighted in [1]). As visualized in the results of Section 4.1, the distribution of the patterns is able to separate OCs with different RS power levels; together with the parameters discussed above, the relationship between the extracted feature patterns and the physical behavior of the system is confirmed.

5. Conclusion

This work has introduced a framework for assessing and interpreting waveform distortion using two different railway power systems as examples. It utilizes unsupervised DL and clustering on 2-D images containing VI diagrams from measurements of railway pantograph quantities. The methodology was applied to data from two ERSs operating at 16.7 Hz and 50 Hz, showcasing its potential for waveform distortion studies. Another peculiar point is the use of VI diagrams (aka Lissajous diagrams) rather than frequency spectra. The VAE enables automatic feature extraction from the VI diagrams, providing valuable insight into the interactions between RS and the power supply grid. The cluster technique further segregates these features, revealing hidden patterns.

The proposed method is not just a theoretical concept, but a practical tool, that can uncover patterns in the 2-D representation of the time-domain admittance. This allows inferences about the sub-second variation of the RS pantograph voltage and current and the related distortion spectra. The patterns identified at the clustering step of the method can be associated with OCs, traction and braking, with different operating points in terms of current intensity. This practical application was validated by the visualization

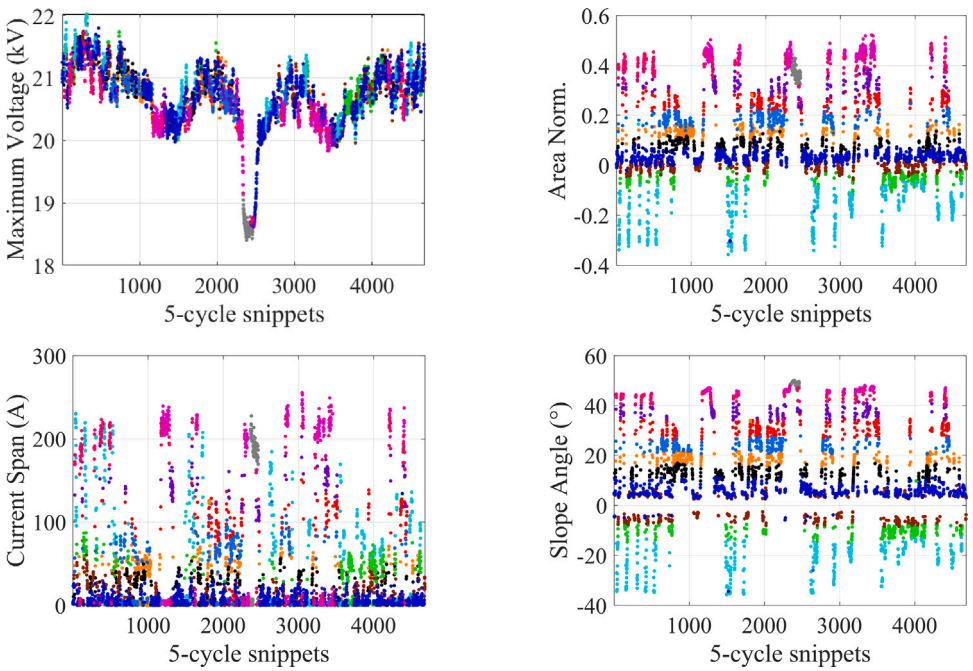

Fig. 17. Distribution of physical parameters extracted from the VI diagrams and the feature patterns based on clusters (figure legends based on Fig. 9): maximum voltage V_{max} (top left), normalized area A (top right), current span $I_{max} - I_{min}$ (bottom left), and slope angle ξ (bottom right).

of the fundamental current phase angle and amplitude, indicating the different states for each cluster, as well as by crosschecking with other parameters with physical meaning, such as the VI trajectory loop area and the slope angle. The ability to identify these patterns is particularly advantageous and challenging in ERSs, where the dynamic aspects of the load and its OCs can lead to quite variable scenarios of absorbed current and waveform distortion.

The accuracy of the method has been also quantitatively verified by means of the mean square reconstruction error (never larger than 1.5% and equal to 0.31% and 0.33% on average for the Swiss and French case, respectively). The t-SNE visualization confirms that overlapping of clusters is negligible, with a percentage of "misplaced" cluster points of 2.18% and 2.50%, again for the Swiss and French case, respectively. On top of that, the computation time for the VAE prediction was evaluated, to pave the way to future implementations.

The results also highlight inferences from the clusters, containing information about harmonic and supraharmonic distortion for what regards the emissions and interaction with the supply grid. The emission characteristics of the onboard converters, low-order harmonics, switching frequency signatures, and their dependency on OCs were identified. The results also demonstrate that voltage spectra patterns for harmonics and supraharmonics show variability of patterns regarding background distortion and impedance changes.

Additionally, the change of the impedance $Z_h = V_h/I_h$ between different OCs and due to line resonances is discussed and demonstrated. The high-frequency impedance values showed to be a suitable added informationto separate patterns found by the method within similar OCs. Z_h values at selected frequencies in the kHz range may vary by as much as 30% between two clusters (like no. 11 and 12 for the Swiss case), yet belonging to the same OC, thus further demonstrating that the final selection of clusters is physically reasonable and justified.

The proposed method was verified in the challenging conditions of the electrified railway dynamic loads for two different sets of experimental results from two countries with different types of RS and power supply architecture. It is thus extendable to a wide range of industrial contexts, featuring harmonic and supraharmonic distortion due to both AC voltage rectification and static power conversion. The possible applications are diagnostics and anomaly detection, characterization of invasiveness of loads in terms of harmonic and supraharmonic distortion during their operation, and in general non-intrusive load monitoring. It is underlined once more that patterns were clustered based on a combination of features, not limiting them to e.g. current or voltage spectrum components, or impedance values, thus ensuring more flexibility with respect to this range of applications and related peculiarities.

Lastly, the methodology trade-offs were discussed, including an overview of alternatives for clustering algorithms and dimensional reduction methods. There is a large range of newly proposed approaches and a direct evaluation of all is a complex task, also because there are not so many publications on applications, proposing sound and suitable performance metrics. This work thus provides useful insights on the verification that results are accurate and physically reasonable. This paves the way to improvement and future directions of research.

CRediT authorship contribution statement

Rafael S. Salles: Conceptualization, Methodology, Software, Validation, Formal analysis, Investigation, Data curation, Writing – original draft, Visualization. **Roger A. De Oliveira:** Conceptualization, Methodology, Investigation, Writing – review & editing. **Sarah K. Rönnberg:** Conceptualization, Methodology, Investigation, Resources, Writing – review & editing, Supervision, Project administration. **Andrea Mariscotti:** Conceptualization, Methodology, Investigation, Writing – review & editing, Visualization.

Declaration of competing interest

The authors declare that they have no known competing financial interests or personal relationships that could have appeared to influence the work reported in this paper.

Data availability

The data is available in a refereed manuscript.

References

[1] Mariscotti A. Non-intrusive load monitoring applied to AC railways. Energies 2022;15(11):4141. http://dx.doi.org/10.3390/en15114141, URL https://www.mdpi.com/1996-1073/15/11/4141.

[2] Femine AD, Gallo D, Giordano D, Landi C, Luiso M, Signorino D. Power quality assessment in railway traction supply systems. IEEE Trans Instrum Meas 2020;69(5):2355–66. http://dx.doi.org/10.1109/TIM.2020.2967162, URL https://ieeexplore.ieee.org/document/8962225/.

[3] Salles RS, Rönnberg SK. Review of waveform distortion interactions assessment in railway power systems. Energies 2023;16(14):5411. http://dx.doi.org/10.3390/en16145411, URL https://www.mdpi.com/1996-1073/16/14/5411.

[4] Hu H, He Z, Li X, Wang K, Gao S. Power-quality impact assessment for high-speed railway associated with high-speed trains using train timetable —part I: Methodology and modeling. IEEE Trans Power Deliv 2016;31(2):693–703. http://dx.doi.org/10.1109/TPWRD.2015.2472994, URL http://ieeexplore.ieee.org/document/7293225/.

[5] Hu H, He Z, Wang K, Ma X, Gao S. Power-quality impact assessment for high-speed railway associated with high-speed trains using train timetable —part II: Verifications, estimations and applications. IEEE Trans Power Deliv 2016;31(4):1482–92. http://dx.doi.org/10.1109/TPWRD.2015.2472961, URL https://www.scopus.com/inward/record.uri?eid=2-s2.0-84979967827&doi=10.1109%2FTPWRD.2015.2472961&partnerID=40&md5=f93dc2e80032cf740ab03afeda27bfe4.

[6] Gao S, Li X, Ma X, Hu H, He Z, Yang J. Measurement-based compartmental modeling of harmonic sources in traction power-supply system. IEEE Trans Power Deliv 2017;32(2):900–9. http://dx.doi.org/10.1109/TPWRD.2016.2578962, URL http://ieeexplore.ieee.org/document/7488255/.

[7] Mariscotti A, Sandrolini L. Detection of harmonic overvoltage and resonance in AC railways using measured pantograph electrical quantities. Energies 2021;14(18):5645. http://dx.doi.org/10.3390/en14185645.

[8] Song Y, Xiao D, Pan P, Chen H, Hu H, He Z. Measurement-based wideband model and electric parameter extraction of railway traction power system. IEEE Trans Transp Electrification 2023;9(1):1483–97. http://dx.doi.org/10.1109/TTE.2022.3170045, URL https://www.scopus.com/inward/record.uri?eid=2-s2.0-85129591519&doi=10.1109%2FTTE.2022.3170045&partnerID=40&md5=df915f05d4f1fb749b42e2ec8d4ffbd5.

[9] EN50388. Railway Applications —Power supply and rolling stock —Technical criteria for the coordination between power supply (substation) and rolling stock to achieve interoperability. 2012, CENELEC, Brussels, Belgium.

[10] EN50163. Railway Applications —Supply voltages of traction systems. 2020, CENELEC, Brussels, Belgium.

[11] Zhao L, Li M. Probability distribution modeling of the interference of the traction current in track circuits. J Theor Appl Inf Technol 2012;46(1):125–31.

[12] Serdiuk T, Havryliuk V, Feliziani M, Serdiuk K. Propagation of harmonics of return traction current in rail lines. In: 2019 international symposium on electromagnetic compatibility - EMC EUROPE. IEEE; 2019, p. 550–5. http://dx.doi.org/10.1109/EMCEurope.2019.8872092, URL https://ieeexplore.ieee.org/document/8872092/.

[13] Mariscotti A. Direct measurement of power quality over railway networks with results of a 16.7-Hz network. IEEE Trans Instrum Meas 2011;60(5):1604–12. http://dx.doi.org/10.1109/TIM.2010.2089170, URL http://ieeexplore.ieee.org/document/5634105/.

[14] Seferi Y, Blair SM, Mester C, Stewart BG. Power quality measurement and active harmonic power in 25 kV 50 Hz AC railway systems. Energies 2020;13(21). http://dx.doi.org/10.3390/en13215698, URL https://www.scopus.com/inward/record.uri?eid=2-s2.0-85105532945&doi=10.3390%2Fen13215698&partnerID=40&md5=1adb972797a22a61162db4b720981e0e.

[15] Mariscotti A. Experimental characterisation of active and non-active harmonic power flow of AC rolling stock and interaction with the supply network. IET Electr Syst Transp 2021;11(2):109–20. http://dx.doi.org/10.1049/els2.12009, URL https://onlinelibrary.wiley.com/doi/10.1049/els2.12009.

[16] Panoiu M, Panoiu C, Mezinescu S, Militaru G, Baciu I. Machine learning techniques applied to the harmonic analysis of railway power supply. Mathematics 2023;11(6). http://dx.doi.org/10.3390/math11061381, URL https://www.scopus.com/inward/record.uri?eid=2-s2.0-85151357502&doi=10.3390%2Fmath11061381&partnerID=40&md5=6009bfc3292fd0c87db7b20ddc094014.

[17] Gonzalez-Jimenez D, Del-Olmo J, Poza J, Garramiola F, Madina P. Data-driven low-frequency oscillation event detection strategy for railway electrification networks. Sensors 2022;23(1):254. http://dx.doi.org/10.3390/s23010254, URL https://www.mdpi.com/1424-8220/23/1/254.

[18] Asheibi A, Stirling D, Sutanto D. Analyzing harmonic monitoring data using supervised and unsupervised learning. IEEE Trans Power Deliv 2009;24(1):293–301. http://dx.doi.org/10.1109/TPWRD.2008.2002654, URL https://ieeexplore.ieee.org/document/4729797/.

[19] Ge C, Oliveira RAD, Gu IYH, Bollen MHJ. Unsupervised deep learning and analysis of harmonic variation patterns using big data from multiple locations. Electr Power Syst Res 2021;194:107042. http://dx.doi.org/10.1016/j.epsr.2021.107042, URL https://www.sciencedirect.com/science/article/pii/S0378779621000225.

[20] de Oliveira RA, Ravindran V, Ronnberg SK, Bollen MHJ. Deep learning method with manual post-processing for identification of spectral patterns of waveform distortion in PV installations. IEEE Trans Smart Grid 2021;12(6):5444–56. http://dx.doi.org/10.1109/TSG.2021.3107908, URL https://ieeexplore.ieee.org/document/9523598/.

[21] Salles RS, de Oliveira RA, Ronnberg SK, Mariscotti A. Analytics of waveform distortion variations in railway pantograph measurements by deep learning. IEEE Trans Instrum Meas 2022;71:1–11. http://dx.doi.org/10.1109/TIM.2022.3197801, URL https://ieeexplore.ieee.org/document/9853622/.

[22] Liu H, Hussain F, Shen Y, Arif S, Nazir A, Abubakar M. Complex power quality disturbances classification via curvelet transform and deep learning. Electr Power Syst Res 2018;163:1–9. http://dx.doi.org/10.1016/j.epsr.2018.05.018, URL https://linkinghub.elsevier.com/retrieve/pii/S0378779618301561.

[23] Kumar LA, Indragandhi V, Selvamathi R, Vijayakumar V, Ravi L, Subramaniyaswamy V. Design, power quality analysis, and implementation of smart energy meter using internet of things. Comput Electr Eng 2021;93:107203. http://dx.doi.org/10.1016/j.compeleceng.2021.107203, URL https://linkinghub.elsevier.com/retrieve/pii/S0045790621001993.

[24] Samanta IS, Rout PK, Swain K, Cherukuri M, Mishra S. Power quality events recognition using enhanced empirical mode decomposition and optimized extreme learning machine. Comput Electr Eng 2022;100:107926. http://dx.doi.org/10.1016/j.compeleceng.2022.107926, URL https://linkinghub.elsevier.com/retrieve/pii/S0045790622002075.

[25] de Oliveira RA, Bollen MH. Deep learning for power quality. Electr Power Syst Res 2023;214:108887. http://dx.doi.org/10.1016/j.epsr.2022.108887, URL https://linkinghub.elsevier.com/retrieve/pii/S0378779622009385.

[26] Yan J, Cheng Y, Wang Q, Liu L, Zhang W, Jin B. Transformer and graph convolution-based unsupervised detection of machine anomalous sound under domain shifts. IEEE Trans Emerg Top Comput Intell 2024;8(4):2827–42. http://dx.doi.org/10.1109/TETCI.2024.3377728, URL https://ieeexplore.ieee.org/document/10489914/.

[27] Dong G, Liao G, Liu H, Kuang G. A review of the autoencoder and its variants: A comparative perspective from target recognition in synthetic-aperture radar images. IEEE Geosci Remote Sens Mag 2018;6(3):44–68. http://dx.doi.org/10.1109/MGRS.2018.2853555, URL https://ieeexplore.ieee.org/document/8474425/.

[28] Takiddin A, Ismail M, Zafar U, Serpedin E. Deep autoencoder-based anomaly detection of electricity theft cyberattacks in smart grids. IEEE Syst J 2022;16(3):4106–17. http://dx.doi.org/10.1109/JSYST.2021.3136683, URL https://ieeexplore.ieee.org/document/9674027/.

[29] Ye M, Chen J, Xiong F, Qian Y. Learning a deep structural subspace across hyperspectral scenes with cross-domain VAE. IEEE Trans Geosci Remote Sens 2022;60:1–13. http://dx.doi.org/10.1109/TGRS.2022.3142941, URL https://ieeexplore.ieee.org/document/9680683/.

[30] Ibrahim R, Zemouri R, Tahan A, Kedjar B, Merkhouf A, Al-Haddad K. Fault detection based on vibration measurements and variational autoencoder-desirability function. IEEE Open J Ind Appl 2024;5:106–16. http://dx.doi.org/10.1109/OJIA.2024.3380249, URL https://ieeexplore.ieee.org/document/10478716/.

[31] Bongiorno J. Induced touch voltage in wayside cables of AC railways caused by traction supply transients. Electr Eng 2023;105(1):13–24. http://dx.doi.org/10.1007/s00202-022-01645-x, URL https://link.springer.com/10.1007/s00202-022-01645-x.

[32] Brenna M, Foiadelli F, Zaninelli D. Electrical railway transportation systems. IEEE press series on power and energy systems, Wiley; 2018, URL https://books.google.se/books?id=ZbVIDwAAQBAJ.

[33] Kiessling F, Puschmann R, Schmieder A, Schneider E. Contact lines for electric railways: Planning, design, implementation, maintenance. Wiley; 2018, URL https://books.google.se/books?id=inVGDwAAQBAJ.

[34] Femine AD, Gallo D, Landi C, Luiso M. Discussion on DC and AC power quality assessment in railway traction supply systems. In: 2019 IEEE international instrumentation and measurement technology conference (i2MTC). IEEE; 2019, p. 1–6. http://dx.doi.org/10.1109/I2MTC.2019.8826869, URL https://ieeexplore.ieee.org/document/8826869/.

[35] Giordano D, Clarkson P, Gamacho F, van den Brom H, Donadio L, Fernandez-Cardador A, et al. Accurate measurements of energy, efficiency and power quality in the electric railway system. In: Conference on precision electromagnetic measurements (CPEM 2018). IEEE; 2018, http://dx.doi.org/10.1109/cpem.2018.8500811.

[36] Mariscotti A. Impact of harmonic power terms on the energy measurement in ac railways. IEEE Trans Instrum Meas 2020;69(9):6731–8. http://dx.doi.org/10.1109/tim.2020.2992167.

[37] Lam H, Fung G, Lee W. A novel method to construct taxonomy electrical appliances based on load signaturesof. IEEE Trans Consum Electron 2007;53(2):653–60. http://dx.doi.org/10.1109/TCE.2007.381742, URL http://ieeexplore.ieee.org/document/4266955/.

[38] Hassan T, Javed F, Arshad N. An empirical investigation of V-I trajectory based load signatures for non-intrusive load monitoring. IEEE Trans Smart Grid 2014;5(2):870–8. http://dx.doi.org/10.1109/TSG.2013.2271282, URL http://ieeexplore.ieee.org/document/6575197/.

[39] Diaz-Rozo J, Bielza C, Larranaga P. Clustering of data streams with dynamic Gaussian mixture models: An IoT application in industrial processes. IEEE Internet Things J 2018;5(5):3533–47. http://dx.doi.org/10.1109/JIOT.2018.2840129, URL https://ieeexplore.ieee.org/document/8364530/.

[40] der Maaten L, Hinton G. Visualizing data using t-SNE. J Mach Learn Res 2008;9(11).

[41] Mariscotti A. Data sets of measured pantograph voltage and current of European AC railways. Data Brief 2020;30:105477. http://dx.doi.org/10.1016/j.dib.2020.105477.

[42] Min E, Guo X, Liu Q, Zhang G, Cui J, Long J. A survey of clustering with deep learning: From the perspective of network architecture. IEEE Access 2018;6:39501–14. http://dx.doi.org/10.1109/ACCESS.2018.2855437, URL https://ieeexplore.ieee.org/document/8412085/.

[43] Valero S, Agullo F, Inglada J. Unsupervised learning of low dimensional satellite image representations via variational autoencoders. In: 2021 IEEE international geoscience and remote sensing symposium IGARSS. IEEE; 2021, p. 2987–90. http://dx.doi.org/10.1109/IGARSS47720.2021.9554661, URL https://ieeexplore.ieee.org/document/9554661/.

[44] Zhu W. Improving the applicability of variational deep embedding in unsupervised large-scale data clustering IT NV - 20086, [Ph.D. thesis], Department of Information Technology, Mathematics and Computer Science, Disciplinary Domain of Science and Technology, Uppsala University; 2020, p. 73, URL: http://uu.diva-portal.org/smash/get/diva2:1541360/FULLTEXT01.pdf http://urn.kb.se/resolve?urn=urn:nbn:se:uu:diva-439300.

[45] An J, Cho S. Variational autoencoder based anomaly detection using reconstruction probability. In: Special lecture on IE 2. 2015, URL https://api.semanticscholar.org/CorpusID:36663713.

[46] Kingma DP, Welling M. Auto-encoding variational Bayes. 2013, arXiv preprint arXiv:1312.6114.

[47] Varadarajan V, Garg D, Kotecha K. An efficient deep convolutional neural network approach for object detection and recognition using a multi-scale anchor box in real-time. Future Internet 2021;13(12):307. http://dx.doi.org/10.3390/fi13120307, URL https://www.mdpi.com/1999-5903/13/12/307.

[48] Mathworks. Choose cluster analysis method. 2023, URL https://www.mathworks.com/help/stats/choose-cluster-analysis-method.html#mw_6a5fcefd-1f9a-479b-bb8f-2160554b0808.

[49] Géron A. Hands-on machine learning with scikit-learn and TensorFlow: Concepts, tools, and techniques to build intelligent systems. O'Reilly Media; 2017, URL https://books.google.se/books?id=bRpYDgAAQBAJ.

[50] Jones J, Paine N. K-means and Gaussian mixture models. In: Medium. 2021, URL https://towardsdatascience.com/clustering-out-of-the-black-box-5e8285220717.

[51] Gao CX, Dwyer D, Zhu Y, Smith CL, Du L, Filia KM, et al. An overview of clustering methods with guidelines for application in mental health research. Psychiatry Res 2023;327:115265. http://dx.doi.org/10.1016/j.psychres.2023.115265, URL https://linkinghub.elsevier.com/retrieve/pii/S0165178123002159.

[52] Hand DJ, McLachlan GJ, Basford KE. Mixture models: Inference and applications to clustering. Appl Stat 1989;38(2):384. http://dx.doi.org/10.2307/2348072, URL https://www.jstor.org/stable/10.2307/2348072?origin=crossref.

[53] IEC61000-4-7. Electromagnetic compatibility (EMC) —part 4-7: Testing and measurement techniques —general guide on harmonics and interharmonics measurements and instrumentation, for power supply systems and equipment connected thereto. 2002.

[54] Gaul A. Function call overhead benchmarks with MATLAB, Octave, Python, Cython and C. 2012, arXiv arXiv:1202.2736.

[55] Bollen MH, Gu IY, Santoso S, Mcgranaghan MF, Crossley PA, Ribeiro MV, et al. Bridging the gap between signal and power. IEEE Signal Process Mag 2009;26(4):12–31. http://dx.doi.org/10.1109/MSP.2009.932706, URL https://ieeexplore.ieee.org/document/5174495/.

[56] Ester M, Kriegel H-P, Sander J, Xu X. A density-based algorithm for discovering clusters in large spatial databases with noise. In: KDD'96: proceedings of the second international conference on knowledge discovery and data mining. Portland, Oregon: AAAI Press; 1996, p. 226–31. http://dx.doi.org/10.5555/3001460.3001507.

[57] Fukunaga K, Hostetler L. The estimation of the gradient of a density function, with applications in pattern recognition. IEEE Trans Inform Theory 1975;21(1):32–40. http://dx.doi.org/10.1109/TIT.1975.1055330, URL https://ieeexplore.ieee.org/document/1055330/.

[58] Yang L, Zhang Z, Song Y, Hong S, Xu R, Zhao Y, et al. Diffusion models: A comprehensive survey of methods and applications. ACM Comput Surv 2023;56(4):1–39.

[59] Ho J, Jain A, Abbeel P. Denoising diffusion probabilistic models. Adv Neural Inf Process Syst 2020;33:6840–51.